Supporting Information

Make It Stereoscopic: Interfacial Design for Full-Temperature Adaptive Flexible Zinc-Air Batteries

Zengxia Pei,[1] Luyao Ding,[1] Cheng Wang, Qiangqiang Meng, Ziwen Yuan, Zheng Zhou, Shenlong Zhao,* Yuan Chen**

Experimental Section

***Synthesis of Polypyrrole nanowire arrays (PPy NAs) precursor*:** PPy NAs were synthesized by a galvanostatic electrodeposition method using a three-electrode configuration with concentrate nitric acid pre-treated carbon cloth (CC), platinum mesh, and saturated calomel electrode as the working electrode, counter electrode, and reference electrode, respectively. Specifically, the electrolyte was prepared by dissolving 0.388 g sodium p-toluenesulfonate into 50 mL 1 M phosphate-buffered solution (pH=7), then 500 μL of pyrrole monomer was added under stirring at 0 °C. A piece of CC (1 × 4 cm) was immersed into the electrolyte (with an effective geometric area of 1 × 3 cm). The electrodeposition of the PPy NAs was achieved by applying a constant current of 8 mA to CC for 30 min. All operations were conducted at 0 °C. After that, the PPy NAs/CC was thoroughly washed and dried at 60 °C.

Synthesis of PPy nanofilm precursor: the PPy nanofilm was synthesized by a potentiostat electrodeposition method using the same three-electrode configuration. For the electrolyte, 500 μL of pyrrole monomer was added into 50 mL water containing 0.03 M sodium p-toluenesulfonate and 0.01 M p-toluenesulfonic acid. A piece of CC (1 × 4 cm) was immersed into the electrolyte (with an effective geometric area of 1 × 3 cm). A constant potential of 0.8 V was applied to CC for about 15-20 min. Note the deposition time was controlled to allow a similar deposited PPy amount (based on the charge passed for the electrochemical deposition). After that, the PPy nanofilm/CC was thoroughly washed and dried at 60 °C.

Synthesis of FeCo-P/N-C-F or FeCo-P/N-C-P electrode: the FeCo-P/N-C-F electrode was synthesized by two-step pyrolysis and phosphorized method. Typically, the PPy NAs/CC was immersed into a mixture solution containing 20 mM $Fe(NO_3)_3$ and 20 mM $Co(CH_3COO)_2$ for 8 h upon mild stirring. After that, one piece of the metal-adsorbed PPy NAs/CC was gently rinsed, dried, and then pyrolyzed under Ar with the presence of 0.5 g dicyandiamide at 500 °C for 1 h, and then at 800 °C for 2h, both with a ramp rate of 5 °C min^{-1}. The resulting electrode was further phosphorized using 0.5 g sodium hypophosphite (put at the upstream of Ar gas flow) upon heating at 350 °C for 2 h, with a ramp rate of 5 °C min^{-1}. The FeCo-P/N-C-F electrode can thus be obtained.

The FeCo-P/N-C-P electrode was synthesized following an identical way to the FeCo-P/N-C-F except that the PPy nanofilm/CC precursor was used. Note the typical loading mass of the FeCo-P/N-C composite (including all the metal compounds and N-doped carbon species) on both the two types of electrodes was determined by a semi-micro balance, which ranged in 0.6 - 0.8 mg cm^{-2} from batch to batch.

Synthesis of other control electrodes: Fe-P/N-C-F or Co-P/N-C-F electrode was fabricated using the method identical to that for FeCo-P/N-C-F electrode, except that the initial PPy

NAs/CC precursor was immersed in 40 mM bare $Fe(NO_3)_3$ or 40 mM bare $Co(CH_3COO)_2$, respectively. The N-C-F or N-C-P electrode was synthesized by directly pyrolyzing PPy NAs/CC or PPy nanofilm/CC precursor at 800 ^oC under Ar for 2 h, respectively.

The noble metal coated electrodes were prepared by coating a desired amount of catalysts onto the N-C-F substrate via a drop-casting method. Typically, 20 mg Pt/C or IrO_2 catalyst was dispersed in a 2 mL H_2O-isopropanol (v : v = 4:1) mixture together with 50 μL Nafion solution (5 wt%). The mixture was sonicated for 30 min to get a homogeneous slurry, and a certain volume of the solution was then pipetted onto N-C-F and dried. The average loading of Pt/C or IrO_2 was controlled at 0.5 mg cm^{-2}.

Physicochemical characterizations: A PANalytical X'Pert Powder X-ray diffractometer analyzed the crystal structure of samples with Cu K_α radiation (λ = 0.15418 nm) operating at 30 kV and 10 mA. The morphology and microstructure of samples were examined by a Hitachi field-emission scanning electron microscope (SEM) and a JEOL-2001F transmission electron microscope (TEM). X-ray photoelectron spectroscopy (XPS) analyses were conducted on a Thermo Fisher ESCALAB 250 photoelectron spectrometer at 1.2×10^{-9} mbar using an Al K_α X-ray beam (1486.6 eV). XPS spectra were charge corrected to the adventitious C 1s peak at 284.5 eV. The hydrogel polyelectrolytes' mechanical tests were conducted on a universal mechanical tester (SUNS, Shenzhen, China) with the tensile and compressing modes. The polyelectrolytes' ionic conductivity was measured using a two-probe AC impedance method on the CHI760D electrochemical workstation. The samples were sandwiched between two stainless steel electrodes and measured at frequencies ranging from 1 to 10^5 Hz with an amplitude of 5 mV. The conductivity was calculated by the equation:

$$\sigma = L / (SR)$$

L is the polyelectrolyte's thickness, S is the cross-sectional area of the polyelectrolyte, and R is the bulk resistance acquired from Nyquist plots.

Electrochemical measurements: all electrochemical measurements were carried out on a CHI 760D electrochemical workstation using a typical three-electrode system. The self-support electrodes were directly used as the working electrode (with an effective working area of 0.5 cm^{-2}), while an Ag/AgCl (filled with 3 M KCl solution) electrode, and a Pt mesh were used as the reference and counter electrode, respectively. For both OER and ORR, the electrolyte was an O_2-saturated 1 M KOH solution. **The recorded potentials were converted to a reference reversible hydrogen electrode (RHE) by calibration** (details see Figure S7).

For OER tests, the LSV curves were obtained at a scan rate of 5 mV s^{-1}. All the curves were iR corrected unless otherwise stated. The electrode was initially swept for 3 cycles to get a stable current. The accelerated degradation test (ADT) was conducted by cycling different electrodes in a potential range of 1.2-1.6 V (vs. RHE) at 100 mV s^{-1}, without iR correction.

For ORR tests, the linear sweep voltammetry (LSV) curves were scanned at 5 mV s^{-1}. A constant O_2 flow (50 mL min^{-1}) was kept purging into the electrolyte. The onset potential (E_{onset}) for ORR is defined as the potential where the reduction current density reaches 1% of the limiting current density. Each catalyst was repeated at least 3 times to exclude possible incidental errors.

To specifically reveal the oxygen reduction path of the free-standing FeCo-P/N-C-F electrode during ORR **(and also to exclude the influence of capacitative current from the carbon cloth substrate), the catalysts were carefully scratched from the FeCo-P/N-C-F electrode**. **The powder was then dispersed into ink, and dropped cast onto a glassy carbon electrode (GCD) with a loading mass of 0.1 mg cm^{-2}**. The catalyst-bearing GCD was integrated with a rotating disk electrode apparatus (Pine Electrochemical set, USA). Polarization curves of the GCD were recorded in the O_2 saturated 1 M KOH electrolyte with a scan rate of 5 mV s^{-1} (**positive scan**) at various rotating speeds from 400 to 2500 rpm. The

transferred electron numbers (n) per O_2 molecule was determined from the Koutecky–Levich (K–L) equation expressed as follows:

$$1/J = 1/J_K + 1/J_L = 1/J_K + 1/(B\omega^{1/2})$$

where J is the measured current density, J_K and J_L are the kinetic-limiting current density and the diffusion-limiting current density, respectively. ω is the rotation rate of the RDE, and B is the Levich slope given by

$$B = 0.2nFC_0D_0^{2/3}v^{-1/6}$$

where n is the number of electrons transferred in the reduction of one O_2 molecule, F is the Faraday constant (F = 96 485 C mol^{-1}), C_0 is the dissolved concentration of O_2 in the solution (7.8×10^{-7} mol cm^{-3} in 1 M KOH), v is the kinematics viscosity of the electrolyte (v = 0.01 cm^2 s^{-1}), and D_0 is the diffusion coefficient of O_2 in 1 M KOH ($D_0 = 1.8 \times 10^{-5}$ cm^2 s^{-1}).[S1] Constant 0.2 is adopted when the rotating speed is in rpm.

The ADT for ORR was conducted by cycling different electrodes in a potential range of 0.6-1.1 V (vs. RHE) at 100 mV s^{-1}, without iR correction.

To determine whether the Fe/Co-Nx-C sites contributed to the ORR performance, poisoning test was conducted. In consideration of the competing reaction between SCN^- and OH^- ions, the FeCo-P/N-C-F electrode was acid-leached and then pre-treated in 0.1 M $HClO_4$ containing 10 mM KSCN to partially block Co/Fe-N_x sites. The electrode was then rinsed thoroughly with DI water and test in 1 M O_2-saturated KOH using RDE protocols.

Synthesis of hydrogel polyelectrolytes: The A-PAA hydrogel polyelectrolyte was synthesized by a free-radical polymerization method. Typically, 7 mL acrylic acid (AA) monomer was dissolved in 10 mL of water, and then a concentrated sodium hydroxide solution (5 mL, 20 M) was added dropwise into the AA solution under stirring at 0 °C. Prior to use, the AA monomer was purified by distillation under reduced pressure and stored in a refrigerator. Note the pre-neutralization step will stabilize the polymer framework, which would otherwise be severely damaged by the subsequent exposure to alkaline solutions. Afterward, 0.1 wt% of N, N'-methylenebisacrylamide (MBAA) was added as a chemical cross-linker, followed by the addition of 0.11 g ammonium persulfate (APS) (as initiator). The solution was stirred for 15 min at 0 °C and was then degassed to remove dissolved O_2 and sealed under N_2. Subsequently, free-radical polymerization was initiated at 65 °C for 2 h. Finally, the as-prepared hydrogel was peeled off, dried, and then soaked in a mixture of KOH (30 wt.%) with/without $Zn(Ac)_2$ (0.2 M) for a specific time. The KOH-filled polyelectrolyte was wipe-dried with paper tissues and used for the following tests. The as-synthesized A-PAA hydrogel has an average water content of 60-65 wt%. The KOH-filled polyelectrolyte has a total solution (KOH+water) content of 60-70 wt% unless otherwise stated.

Assembly of liquid and flexible ZABs: for liquid ZABs, the FeCo-P/N-C-F was first wetted by PTFE solution (1 wt%) according to a reported method.[S2] Specifically, the electrode was soaked in PTFE solution for 5 min, which was then heated at 200 °C for 30 min in Ar atmosphere to get the well-balanced air-cathode. After that, the treated electrode was pressed together with a gas diffusion layer (GDL) to work as a cathode. The noble metal counterpart was fabricated by drop-casting Pt/C+IrO_2 (with equal weight ratio) mixture onto the hydrophilic side of the GDL, with a loading mass of 0.6 mg cm^{-2} and an effective area of 1 cm^2. A polished Zn foil (0.05 mm thickness) served as an anode, and the electrolyte was 6.0 M KOH with 0.2 M $Zn(Ac)_2$. The measurements of the as-fabricated cell were carried out at room temperature in a static ambient atmosphere (viz., no air purging), using a LANHE multi-channel battery tester.

For flexible ZABs, the FeCo-P/N-C-F or FeCo-P/N-C-P electrode was directly used as an air-cathode after being wetted by PTFE solution (1 wt%). A polished Zn foil (0.05 mm thickness) was used as the anode. The A-PAA hydrogels filled with KOH or KOH+$Zn(Ac)_2$

served as quasi-solid state electrolytes. The flexible ZABs were then assembled by sandwiching the air-cathode and the Zn anode on the polyelectrolyte's two sides. The ZABs were tested at 80, 50, 25, 0, and -30 °C in a constant temperature chamber with a continuous feeding air flow (100 mL min^{-1}). For the tests under 25, 50, and 80 °C, the chamber's humidity was fixed at 60% to simulate the typical natural environment.

Calculation Details

Electrocatalysis part: All the density functional theory (DFT) calculations were performed by Vienna Ab-initio Simulation Package (VASP),[S3] employing the Projected Augmented Wave (PAW) method.[S4] The revised Perdew-Burke-Ernzerhof (RPBE) functional was used to describe the exchange and correlation effects.[S5] The GGA + U calculations are performed using the model proposed by Dudarev et al.,[S6] with the U_{eff} (U_{eff} = Coulomb U – exchange J) values of 3.3 eV and 4 eV for Co and Fe in hydroxide environment, respectively. The CoFeOOH model was constructed with four atomic layers. To simulate the charged CeFeOOH, one unit positive charge was assigned to the whole model frame. For all the geometry optimizations, the cutoff energy was set to be 500 eV. A 2×5×4 Monkhorst-Pack grids[S7] was used to carry out the surface calculations on all the models.

In alkaline conditions, OER occurs via the following elementary steps:

$OH^- + * \rightarrow *OH + e^-$

$*OH + OH^- \rightarrow *O + H_2O + e^-$

$*O + OH^- \rightarrow *OOH + e^-$

$*OOH + OH^- \rightarrow * + O_2 + H_2O + e^-$

where * denotes the active sites on the catalyst surface. Based on the above mechanism, the free energy of three intermediate states, *OH, *O, and *OOH, are important to identify a given material's OER activity. The computational hydrogen electrode (CHE) model[S8] was used to calculate the free energies with applied potential. The free energy of an adsorbed species is defined as

$$\Delta G_{ads} = \Delta E_{ads} + \Delta E_{ZPE} - T\Delta S_{ads}$$

where ΔE_{ads} is the electronic adsorption energy, ΔE_{ZPE} is the zero point energy difference between adsorbed and gaseous species, and $T\Delta S_{ads}$ is the corresponding entropy difference between these two states. The electronic binding energy is referenced as ½ H_2 for each H atom, and (H_2O – H_2) for each O atom, plus the energy of the clean slab. The corrections of zero point energy and entropy of the OER intermediates can be found in Table S1.

Electrolyte part: The first-principles calculations were conducted using generalized gradient approximation (GGA)[S9] and Perdew–Burke–Ernzerhof (PBE)[S10] exchange-correlation functional in DMol3 module of Materials Studio. An all-electron numerical basis set with polarization functions (DNP basis set) with a basis file of 3.5 was employed during calculating. The convergence tolerance was set to 1.0×10^{-5} Ha per atom (1 Ha = 27.211 eV) for energy, 1.0×10^{-6} Ha per atom for the self-consistent field, 2.0×10^{-3} Ha $Å^{-1}$ for maximum force, and 5.0×10^{-3} Å for maximum displacement. The binding energy (E_b) was calculated by the following equation:

$$E_b = E_{total} - E_{polymer} - E_{water}$$

E_{total}, $E_{polymer}$, and E_{water} represent the total energy of the polymer chain combined with H_2O, the energy of the polymer chain, and the energy of H_2O, respectively.

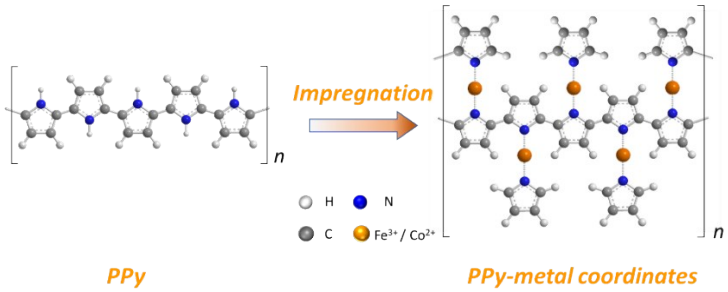

Figure S1. Structure of the PPy precursor and the possible configuration of the PPy-metal complex.

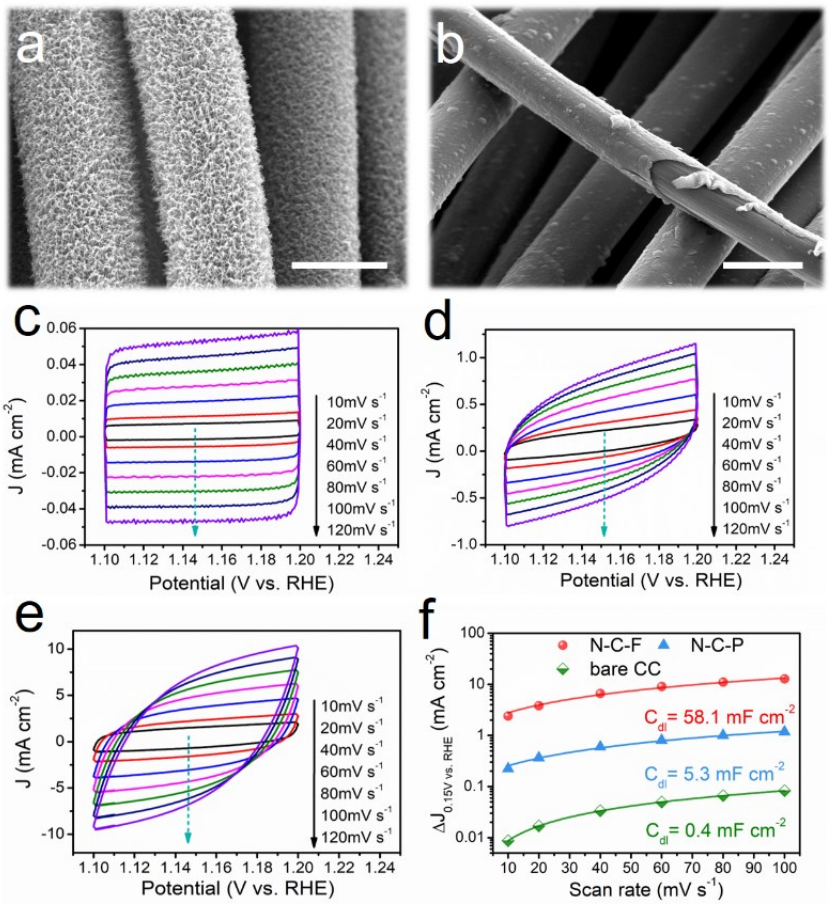

Figure S2. SEM images showing the morphology of (a) PPy nanowires on carbon cloth; (b) PPy nanofilm on carbon cloth. Scale bar: 10 μm in both (a) and (b). CV curves of (c) bare CC; (d) N-C-P; (e) N-C-F recorded between 1.1 and 1.2 V (vs. RHE) at different scan rates. (f) Capacitive current density as a function of scan rates of different samples, with the double-layer capacitance (C_{dl}) values listed.

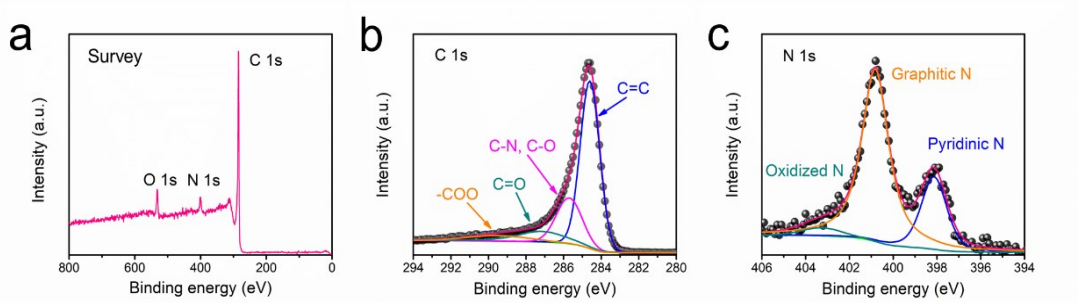

Figure S3. XPS analyses of the pyrolyzed PPy NAs/CC sample: (a) survey spectrum; (b) fitted C 1s core level; (c) fitted N 1s core level.

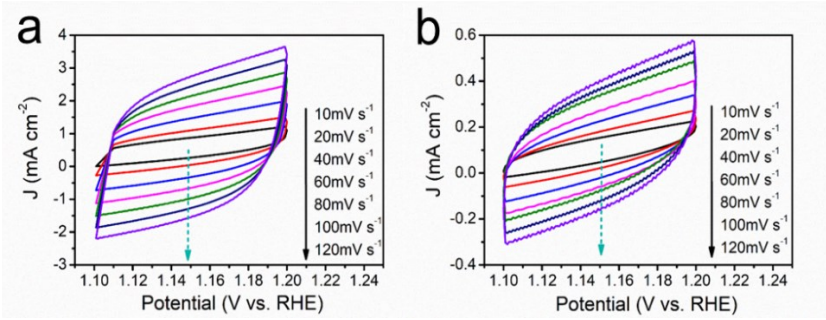

Figure S4. CV curves of (a) FeCo-P/N-C-F and (b) FeCo-P/N-C-P electrodes recorded between 1.1 and 1.2 V (vs. RHE) at different scan rates.

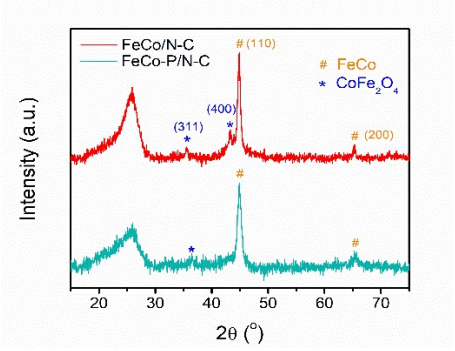

Figure S5. XRD patterns of the pyrolyzed sample before and after phosphorization treatment.

Note 1: The carbon fibers of CC are highly graphitized; thus, the XRD patterns of the metal compounds loaded on CC are concealed by the intense signals from carbon. Therefore, the catalysts were carefully scratched from the free-standing electrodes for XRD characterizations.

As shown in **Figure S5**, after pyrolysis, the FeCo/N-C sample exhibits two main peaks assigned to the FeCo alloy species (Reference code: 03-065-4131), with another two minor peaks indexed to spinel $CoFe_2O_4$ (Reference code: 00-003-0864). This phenomenon is understandable because the surface of these metallic nanoparticles is highly sensitive to exposed atmospheric oxygen and can be easily oxidized in air.[S11] The as-formed surficial metal oxide layer, typically with a thickness of a few nanometers, can prevent the further oxidation of the inner metal cores.[S11b, c] Please note no post-synthetic oxidation procedure was conducted in this work, yet the XRD results imperatively indicate the existence of spinel $CoFe_2O_4$. Further, the XPS analyses toward the chemical state of Fe and Co elements in the as-synthesized FeCo/N-C-F sample were performed. As displayed in **Figure S6**, only oxidized Co^{2+} and Fe^{3+} species were detected, confirming that the FeCo alloy surface will be naturally oxidized in air. Hence, in the initial FeCo/N-C-F sample, the metal species mainly exist as the metallic FeCo alloy core, with a thin layer of $CoFe_2O_4$ oxide shell/surface.

In the subsequent phosphorization process, the phosphine gas (PH_3, generated from hypophosphite) will reduce the surficial metal oxides into metal phosphides.[S12] However, as shown from the XRD result of the phosphorized FeCo-P/N-C-F sample in **Figure S5**, the two peaks of spinel $CoFe_2O_4$ oxide become hazy (the (400) peak almost disappeared), while the two peaks of FeCo were still very strong. Meanwhile, no discernable peaks from metal phosphides were detected. These results suggest the phosphorization process probably occurred only on the surficial $CoFe_2O_4$ layer. Combining XRD and XPS results here and the TEM and XPS analyses in **Figure 1** in the main text, it can be concluded that the metal compounds exist in a core@shell (metal-alloy@metal-oxide/phosphide) structure.

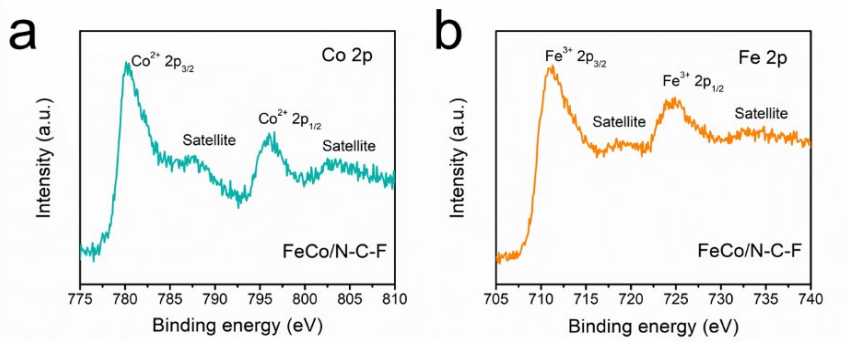

Figure S6. XPS fine spectra of (a) Co 2p and (b) Fe 2p core levels recorded from the as-synthesized FeCo/N-C-F electrode.

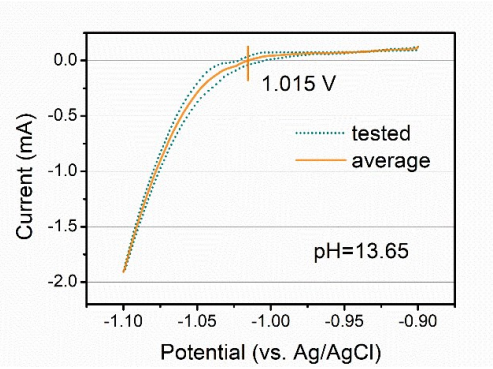

Figure S7. Calibration curves of the reference electrode (Ag/AgCl filled with 3 M KCl solution), tested at 25 °C.

Note 2: Calibration of the reference electrode was performed according to a reported method.[S13] Typically, Pt foil was used as both the working and counter electrodes, and Ag/AgCl served as the reference electrode. The electrolyte was 1 M KOH solution (the same as that in subsequent electrocatalytic tests), which was initially purged with high purity (99.99%) H_2 gas for 30 min. The CV scan was then conducted in the range of -1.10 to -0.90 V, with a scan rate of 1 mV s^{-1} (the H_2 flow was still maintained during the scan). The potential where the average current cross zero was taken as the thermodynamic potential (vs. Ag/AgCl) for hydrogen electrode.

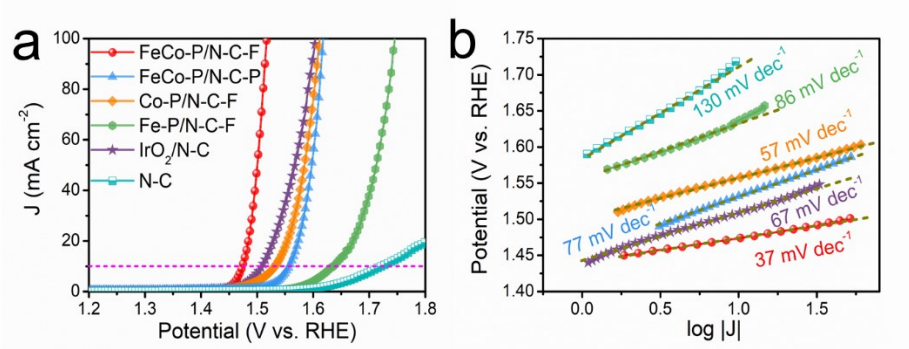

Figure S8. (a) OER polarization curves and (b) corresponding Tafel slopes of different free-standing electrodes in 1 M KOH.

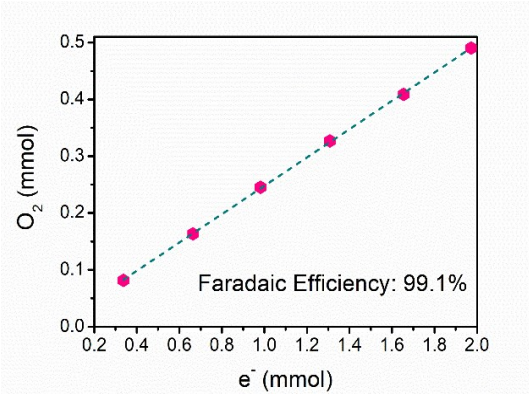

Figure S9. Faradiac efficiency plot showing the evolved oxygen vs. the amount of consumed electrons during the course of electrolysis.

Note 3: Faradiac efficiency was tested using the volumetric method. The produced O_2 over the free-standing FeCo-P/N-C-F electrode (effective area 1.0 cm^{-2}) was accumulated in a graduated tube, which was filled with the electrolyte. Current dominated electrolysis was executed at 10 mA cm^{-2} under ambient conditions (22℃, 1 atm). The time was recorded at every 2 ml of O_2. The collected charges going through the working electrode, in the meantime, were reckoned via current × time. The collected gas was sampled with a Hamilton syringe and detected by using a gas chromatograph to evaluate its purity, which shows the O_2 is the only gaseous product without other impurities.

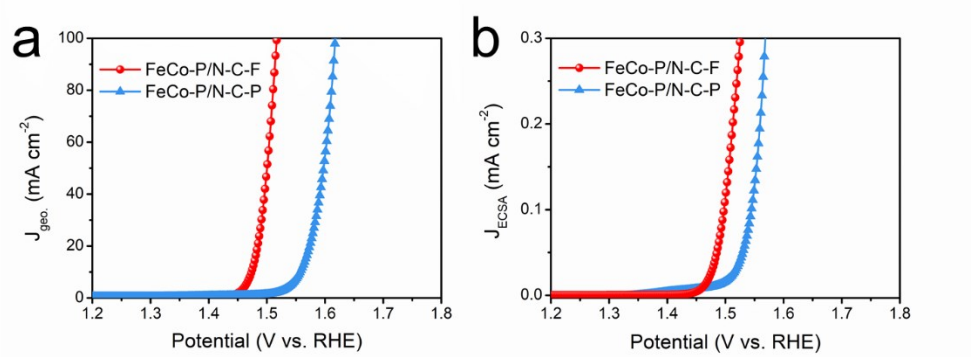

Figure S10. OER current density of the stereoscopic and planar electrodes (a) before and (b) after normalization of their electrochemical surface areas (ECSAs).

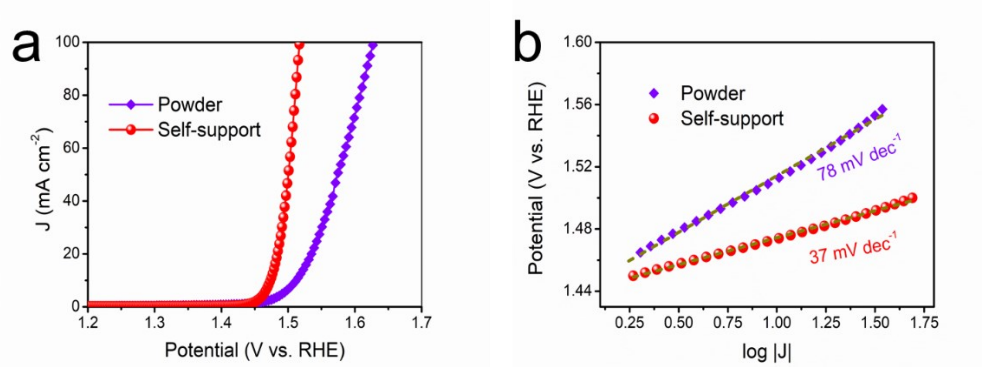

Figure S11. (a) OER polarization curves and (b) corresponding Tafel slopes of the free-standing and scratched powder from FeCo-P/N-C-F electrode in 1 M KOH.

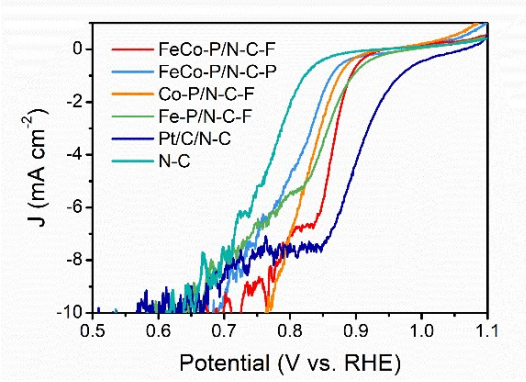

Figure S12. Polarization curves of the free-standing electrodes in static O_2-saturated 1 M KOH solution.

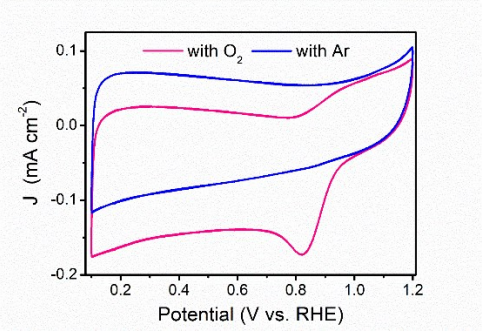

Figure S13. CV curves of the FeCo-P/N-C-F catalyst powder on GCD scanned at 5 mV s^{-1} in O_2- and Ar-saturated 1 M KOH, with a catalyst loading mass of 0.1 mg cm^{-2}.

Note 4: As can be observed from **Figure S13**, the catalyst exhibits an obvious enlarged reduction current in O_2-saturated electrolyte compared with that in Ar-saturated one,

suggesting the intrinsic ORR activity of the catalyst. Actually, the ORR activity of the catalyst was also corroborated in the RDE tests as shown in **Figure S14**.

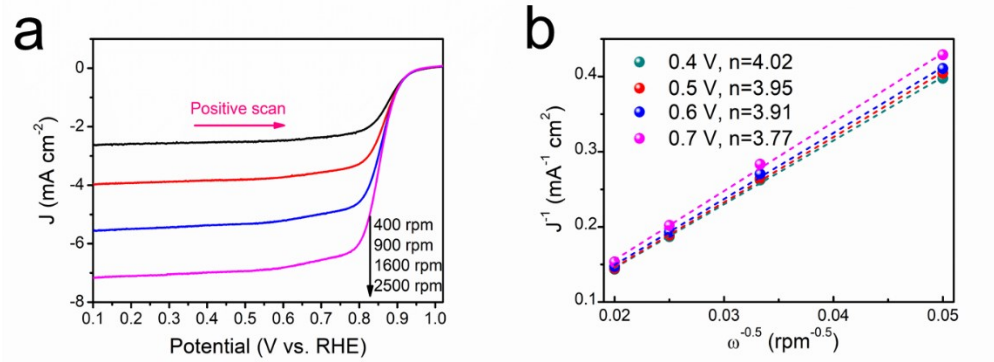

Figure S14. (a) LSV curves of FeCo-P/N-C-F catalyst powder on GCD at different rotation speeds; (b) corresponding K-L plots and the electron transfer numbers.

Note 5: To determine the oxygen reduction path of the catalyst and also to exclude the possible influence of capacitive current from the carbon cloth substrate, the catalysts were carefully scratched from FeCo-P/N-C-F electrode. The collected powder was made into an ink, which was further cast onto the GCD with a loading mass of 0.1 mg cm^{-2}. As shown in **Figure S14a**, the reduction current shows a typical rotation speed-dependent character. The sample delivers a limiting reaction current density of 5.6 mA cm^{-2}, with a half-wave potential ($E_{1/2}$) of 0.85 V at the rotation speed of 1600 rpm. The electron transfer number (n) per oxygen molecule was determined to be 3.77- 4.02 in a wide potential range (**Figure S14b**), revealing a nearly direct $4e^-$ reduction pathway for ORR. Therefore, these results confirm that the FeCo-P/N-C-F electrode can exert ORR via a desirable $4e^-$ reduction pathway.

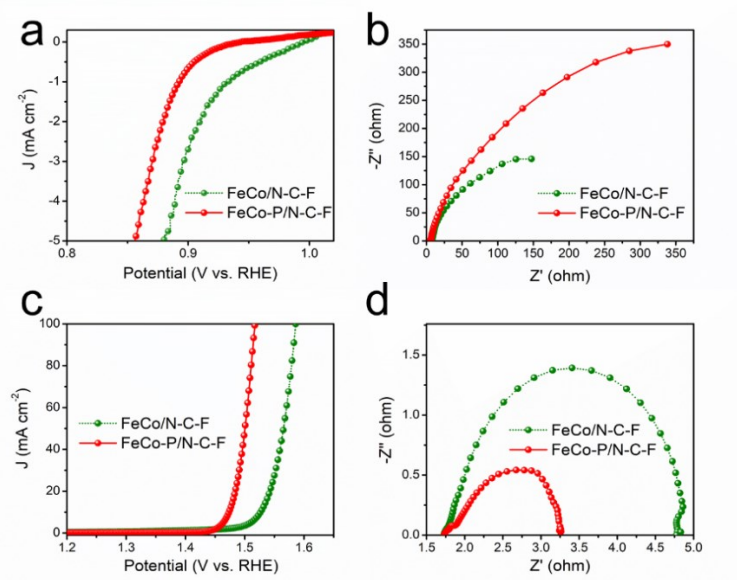

Figure S15. Influences of the phosphorization process on the (a) ORR and (c) OER activities of the stereoscopic electrodes, with the corresponding EIS spectra for (b) ORR and (d) OER. The EIS spectra were recorded at 0.7 and 1.53 V (vs. RHE) for ORR and OER, respectively.

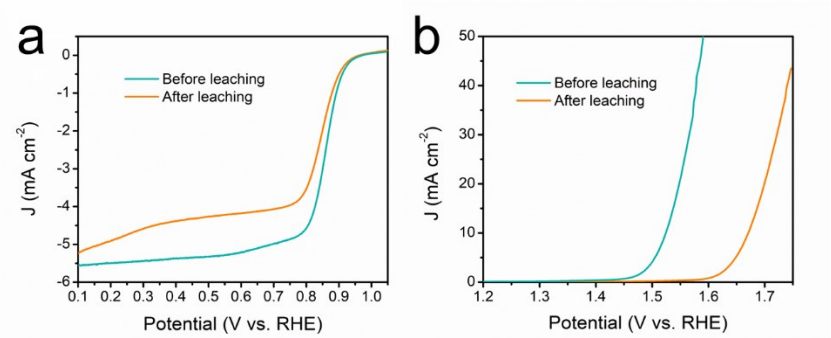

Figure S16. (a) ORR and (b) OER polarization curves of the FeCo-P/N-C-F catalyst powder before and after acid (0.5 M H_2SO_4) leaching. Tested in O_2 saturated 1 M KOH solution at 1600 rpm.

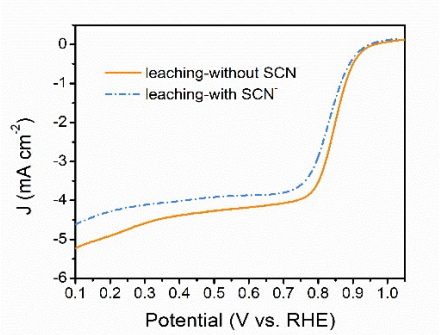

Figure S17. ORR polarization curves of the acid leached FeCo-P/N-C-F catalysts powder before and after poisoning with SCN^-. Tested in O_2 saturated 1M KOH solution at 1600 rpm.

Note 6: To determine the active sites of the FeCo-P/N-C-F electrode, several control tests were conducted. **Figure S15** shows that the phosphorized sample affords enhanced OER activity but obviously decelerated ORR kinetics, suggesting the metal alloy particles (with oxidized surface) might be involved in ORR. **Figure S16** shows that after acid (0.5 M H_2SO_4) etching, the ORR activity of the FeCo-P/N-C-F sample exhibits a moderate decline, while the OER performance shows a substantial degradation. These results confirm that the metal sites contributed to both reactions but predominately to OER. It should be noted that the N-doped carbon and chelating metal-nitrogen (M-N_x) moieties can be very active sites for ORR. Hence, poisoning test was conducted. In consideration of the competing reaction between SCN^- and OH^- ions,[S14] the acid-leached FeCo-P/N-C-F electrode was pre-treated in 0.1 M $HClO_4$ containing 10 mM KSCN to partially block Co/Fe-N_x sites, which was then rinsed thoroughly and measured in 1 M O_2-saturated KOH. **Figure S17** shows that the ORR polarization curve presents obvious shrinkage, suggesting the Co/Fe-N_x sites also contributed to the ORR activity. Taken together, we believe that the ORR activity of the FeCo-P/N-C-F electrode primarily stems from the Co/Fe-N_x and N-doped carbon sites, while the OER performance was mainly contributed by the metal composites (which will be discussed below).

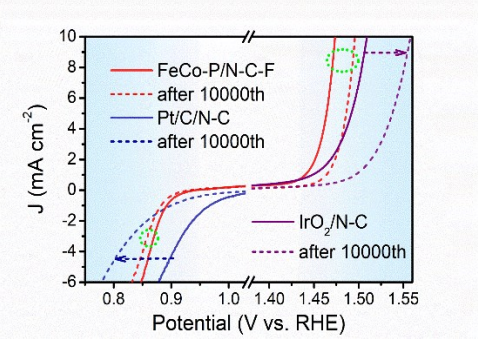

Figure S18. Stability profiles of FeCo-P/N-C-F for ORR and OER compared with Pt/C and IrO_2 loaded on the N-C-F substrate.

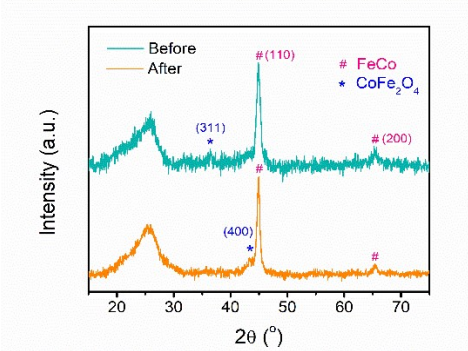

Figure S19. XRD patterns of the FeCo-P/N-C-F electrode before and after OER test.

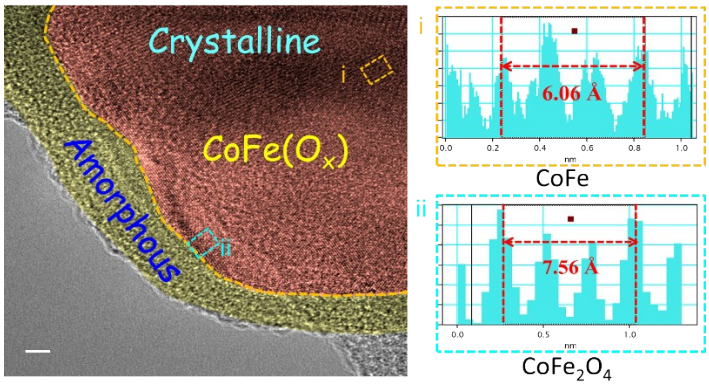

Figure S20. An HRTEM image showing the evolved core@shell structured metal sites after OER, with two magnified regions showing the lattice fringes of CoFe alloy and $CoFe_2O_4$. Scale bar: 2 nm.

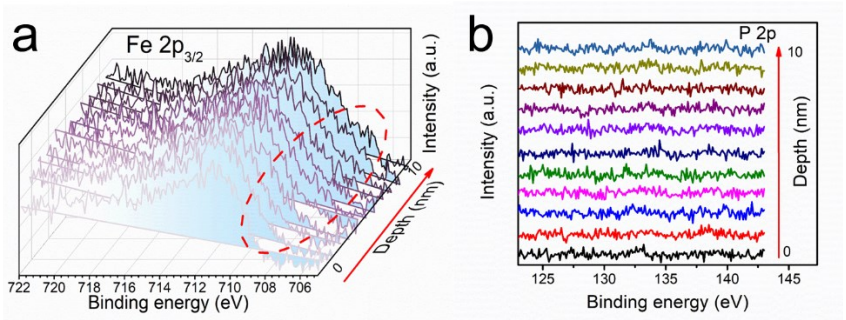

Figure S21. XPS depth analyses of the FeCo-P/N-C-F sample after OER tests: (a) Fe 2p core levels, with the red dashed line showing the gradually exposed signal from inner metallic species; (b) P 2p core levels.

Note 7: The metal phosphides are good pre-catalysts, which would undergo local reconstruction/transformation when applied under oxidative potentials.[S15] To reveal the metal sites' chemical structure after OER, we performed the post-mortem characterizations toward the evolved FeCo-P/N-C-F electrode. XRD results in **Figure S19** suggest the post-OER FeCo-P/N-C-F sample is slightly different from that of the pristine electrode, as evidenced by the distinct trade-off between the signal of (311) and (400) planes. Therefore, the spinel $CoFe_2O_4$ middle layer is more likely to (but might not totally) originate from the oxidative reconstruction (from inner FeCo alloy). Notably, the diffraction peaks of the FeCo alloy are still predominant, highlighting the alloy core hardly goes through reconstruction. This is reasonable since the FeCo alloy parts are not in direct contact with electrolyte; instead, they may contribute to the activity by providing a highway for charge transfer.[S11c, S12, S16] Besides, we have checked the composition of the crystalline region in the HRTEM image of **Figure 2c**. The magnified lattice fringes in **Figure S20** suggest that the outer part of the inner crystalline core exists as spinel $CoFe_2O_4$, while the most interior part is CoFe alloy.

Moreover, XPS depth-profile analyses were performed. The O 1s spectra in **Figure 2d** corroborate that the signal of metal oxyhydroxide (MOOH) species was detected exclusively on surficial layers (<4 nm), while the metal oxide (MO) ones' signal gradually becomes weak but is still discernable in the inner part (until 10 nm depth). On the other hand, the Co and Fe 2p core levels in **Figure 2e, S21a** exhibit that the metal sites' surface contains both MO and MOOH species. Upon etching of the surficial layer by Ar^+ sputtering, obvious peaks with lower binding energy gradually emerged (as highlighted by the dashed circles in **Figure 2e, S21a**), suggesting inner metallic species (viz., FeCo alloy). It should be noted these XPS depth-profile analyses are highly consistent with the TEM observation of the metal site after OER in **Figure 2c**, in which an obvious amorphous outer layer of about 3-6 nm was formed on the inner crystalline core. Simultaneously, no P element was detected (**Figure S21b**) throughout the depth-profile tests. The initial low-valence state P ($P^{\delta-}$) can be oxidized into the high-valence state ($P^{\delta+}$) such as that in phosphate ions (PO_4^{3-}), which is soluble and can be leached away in aqueous electrolytes (like KOH solution in this work).[S12, S17] In a nutshell, the combined XPS (**Figure 1g-i, 2d-e, S6, S21a-b**), HRTEM (**Figure 1d-e, 2c, S20**), and XRD (**S5, S19**) tests suggest that the reconstruction process mainly occurred in the surficial ($(CoFe)_2P$ layer, which evolved into an amorphous CoFeOOH shell; the inner crystalline parts (FeCo alloy and spinel $CoFe_2O_4$) were largely retained. For simplicity, in the manuscript, we

marked the inner crystalline core as $FeCo(O_x)$, hence the metal sites reconstructed into a $FeCo(O)_x$@CoFe-OOH structure. Please note that such a reconstructed crystalline@thin amorphous layer structure is stable during OER, as convinced by some recent similar studies.[S16b, S18] The amorphous metal oxyhydroxide layer, with its small thickness (typically ≤ 5nm), can be substantially affected by the inner core when exerting OER, as discussed below.[S16b, S18b, 18c]

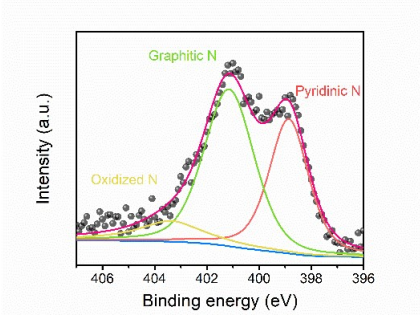

Figure S22. XPS spectrum of N 1s core level of the FeCo-P/N-C-F electrode after OER.

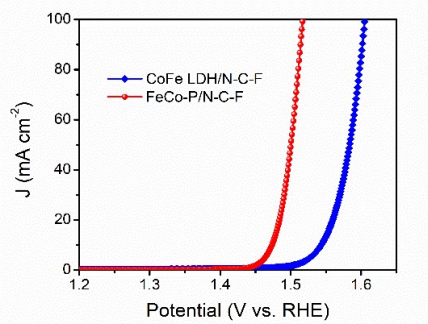

Figure S23. OER polarization curves of the FeCo-P/N-C-F and the control CoFe LDH/N-C-F free-standing electrodes in 1 M KOH.

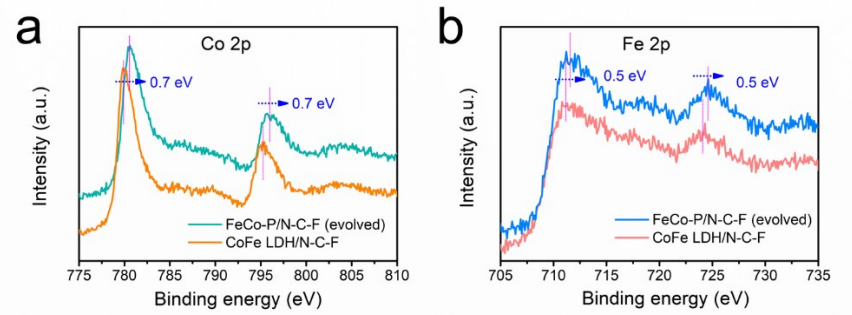

Figure S24. XPS spectra of (a) Co 2p and (b) Fe 2p in the evolved FeCo-P/N-C-F and bare CoFe LHD electrodes.

Note 8: As discussed above, the surface of the metal composite was evolved into an amorphous CeFeOOH layer during OER. The amorphous CoFeOOH species is quite active to OER. Herein, we investigated the intrinsic property of the core@shell structure to reveal the influence of the inner core. XRD (**Figure S19**) and HRTEM (**Figure S20**) results confirm that the outer part of the inner crystalline core exists as spinel $CoFe_2O_4$ layer. It is known that the $CoFe_2O_4$ is a typical p-type semiconductor,[S19] whilst CoFe LDH exhibits n-type behaviors.[S20] The intimate contact of the two species will form a p-n junction on the interface, where the electrons from the n-type side will transfer to the p-type side, making the LDH moiety more positively charged.[S21] To review such an intrinsic charge transfer driven by the build-in field, we performed XPS analyses toward the evolved FeCo-P/N-C-F electrode and controlled CoFe LDH sample. Compared with the bare CoFe LDH (synthesized by a direct electrodeposition method[S20] to avoid using insulative binders), we found the calibrated characteristic peaks of Co 2p and Fe 2p all exhibit positive shifts of around 0.5-0.7 eV (**Figure S24**). The higher binding energy suggests overall higher charged states, which is beneficial for OER.[S18b, 18c, S21, S22] This also explains why the in situ evolved FeCo-P/N-C-F electrode affords much better OER activity than that of the CoFe LDH loaded electrode, as shown in **Figure S23**.

To get an atomic insight into the active sites, DFT calculations were performed. A reported CoFeOOH model was used to simulate the surficial amorphous metal oxyhydroxide layer.[S18b, S21, S22b] As shown in **Figure S25**, the computational results based on the bare CoFeOOH show that on the Co site, the *OOH formation (step III, ΔG_{*OOH} = 1.71 eV) is the rate-determining step (RDS). For the positively charged CoFeOOH, the RDS remained the same but a reduced ΔG_{*OOH} of 1.61 eV is required. In other words, DFT calculations suggest an overpotential of 0.48 V and 0.38 V for bare CoFeOOH and positively charged CoFeOOH, respectively. This result further corroborates that the partially charge-depletion effect from the $CoFe_2O_4$ core is beneficial for the OER activity of surficial CoFeOOH. When Fe site was fixed as the active center, the RDS changed to the initial formation of *OH (step I), but with a much larger ΔG_{*OH} of 2.16 eV and 2.08 eV for bare CoFeOOH and charged CoFeOOH, respectively (**Figure S25-26**). Hence, the Co site is the active site for OER; the unique core@shell structure from the in situ evolved metal sites can render more positive charge on the surficial CoFeOOH layer to further boost its OER kinetics.

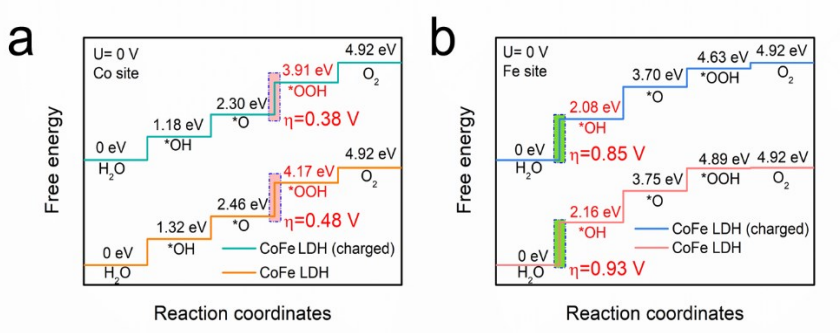

Figure S25. Gibbs free-energy diagram for the four steps of OER on the (a) Co and (b) Fe sites in bare and charged CoFe-LDHs.

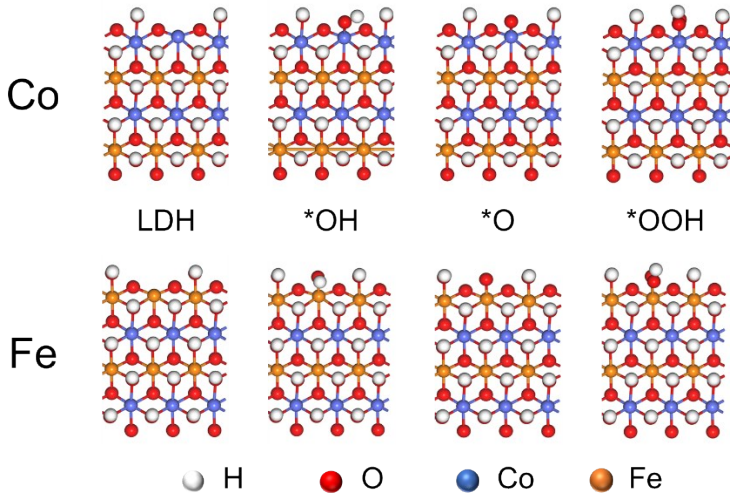

Figure S26. Optimized geometric structures of the bare FeCo LDH, *OH, *O, and *OOH adsorbed Co and Fe sites in FeCo LDH.

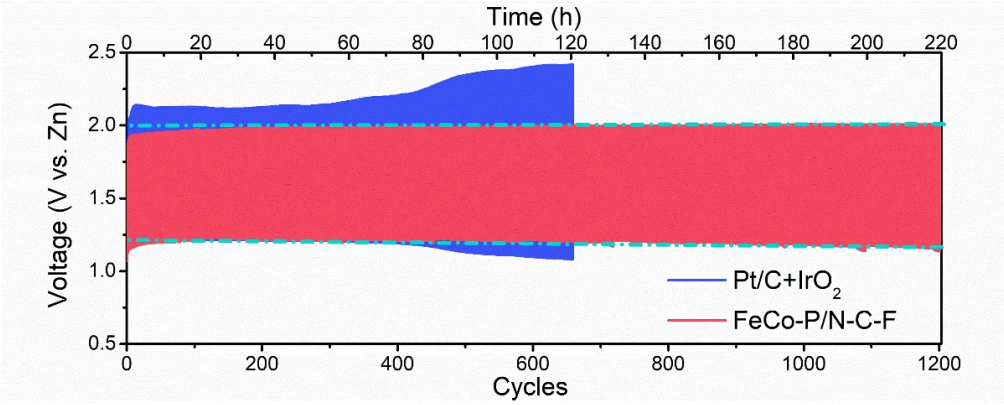

Figure S27. Charging-discharging cycling profiles of the FeCo-P/N-C-F and noble metal mixture (Pt/C+IrO_2) based aqueous ZABs tested at 10 mA cm^{-2} under 25 ^oC.

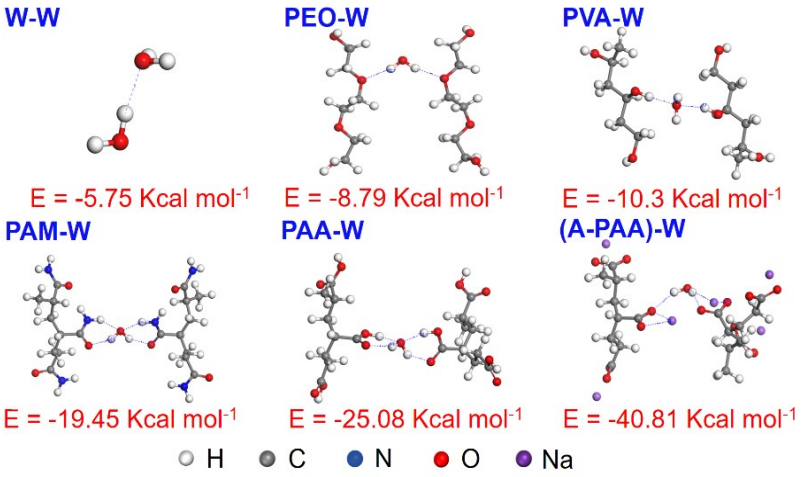

Figure S28. DFT optimized structures of different polymers interacting with water and the corresponding interaction energies.

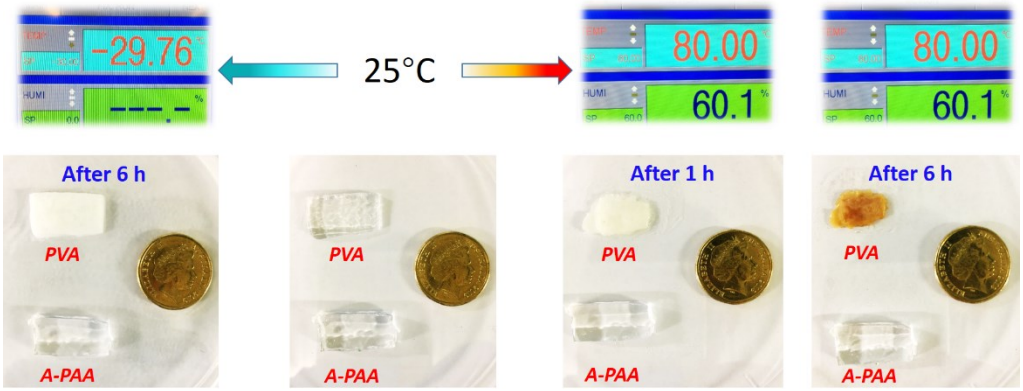

Figure S29. Comparison of the KOH-filled A-PAA and PVA hydrogel after placed in -30 and 80 °C environments.

Note 9: To validate the influence of interaction between water and the terminal groups within polymer backbones on the anti-freezing and anti-drying properties of the hydrogel electrolytes, we compared the temperature adaptability of the A-PAA hydrogel and the most frequently used PVA hydrogel. The PVA hydrogel was synthesized according to a previously reported method.[S23] As shown in **Figure S29**, the as-synthesized PVA hydrogel froze after storing under -30 °C for 6 hours, losing its flexibility. When stored under 80 °C, the PVA hydrogel irreversibly dried out after only 1 h, and its shape showed obvious shrinkage. By contrast, the A-PAA hydrogel could withstand the extreme temperature and well-kept the gel state even after 6 hours. Such remarkable distinctions suggest that the polymer-water interaction can indeed be utilized to render temperature adaptability, which also corroborates the calculation results in **Figure S28**. Further, the A-PAA hydrogel's flexibility remained stable (**Figure 3e, 3f**), while its ionic conductivity could also be well-retained (**Figure 3d, S30**). These results suggest that the A-PAA is a promising polyelectrolyte with excellent temperature adaptability.

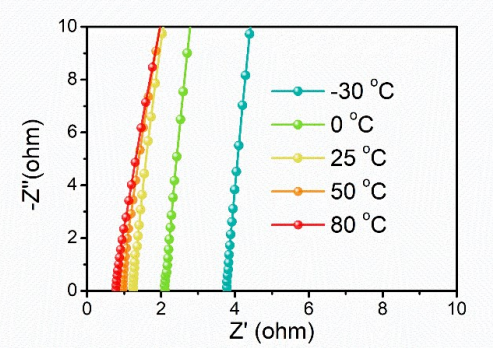

Figure S30. Temperature-dependent resistance of the 30 wt% KOH-filled A-PAA polyelectrolyte. The tested hydrogel is 15 × 10 × 5 mm (length × width × thickness) in size.

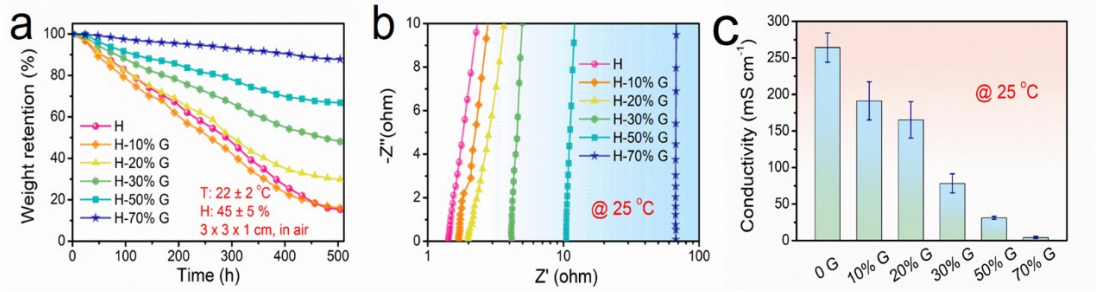

Figure S31. (a) Water retention profiles of the A-PAA hydrogel and different glycerol-water solution filled organohydrogels; (b) EIS spectra of the 30 wt% KOH impregnated A-PAA hydrogel and organohydrogels under 25 °C; (c) corresponding ionic conductivity of the 30wt% KOH impregnated A-PAA hydrogel and organohydrogels from (b). The size of the gels for weight retention was 30 × 30 × 10 mm (length × width × thickness), while that for EIS testing was 15 × 10 × 5 mm.

Note 10: To verify the effectiveness of the organohydrogels as polyelectrolytes for flexible ZABs, the A-PAA hydrogel (H) was first immersed into pure water or different water-glycerol binary solutions until saturation. The glycerol (G) is a typical hygroscopic kosmotrope with low vapor pressure. The weight percent G in the binary solutions varied from 10 to 70%. To accelerate the test, a piece of hydrogel or organohydrogel with large size of 30 × 30 × 10 mm was directly put in an ambient environment without any cover. The weight loss of the gels was then recorded. As shown in **Figure S31a**, after over 500 hours (*ca.* 21 days), the A-PAA can gradually reach equilibrium and still retain 16 wt% of the water. This performance is roughly comparable with the gel impregnated with 10 or 20 wt% of G solution. Due to the hygroscopic nature of G, the binary solution with G weight percent over 30 can obviously improve the water retention capability of the organohydrogel. However, as shown in **Figure S31b** and **S31c**, the introduction of G will lead to a dramatic decrease in the ionic conductivity of the KOH-filled A-PAA polyelectrolytes (that is, A-PAA impregnated with a ternary solution with varied weight ratios between G and 30 wt% KOH aqueous electrolyte). The 70 wt% G impregnated A-PAA polyelectrolyte only affords a small conductivity of 4.6 mS cm^{-1} under 25 °C, about two orders of magnitude smaller than that of the G-free counterpart.

As for the anti-freezing property, the organohydrogel can withstand a frozen temperature around -40 °C after filled with a high G content of 60-70 wt% (**Figure S32a**).[S24] However, as justified above, the anti-freezing performance is at the great sacrifice of the polyelectrolyte's ionic conductivity. In sharp contrast, the 30 wt% KOH-filled A-PAA hydrogel possesses a freezing point down to -33 °C (which is highly comparable with that of the organohydrogels), yet its ionic conductivity is as high as 265 mS cm^{-1} under 25 °C (**Figure S31c, S32b**). Even at -30 °C, the hydrogel polyelectrolyte can afford a conductivity of 90 mS cm^{-1} (**Figure 3d**). The high conductivity is vital to guarantee the electrochemical performance of the flexible ZABs under extreme frozen temperatures.

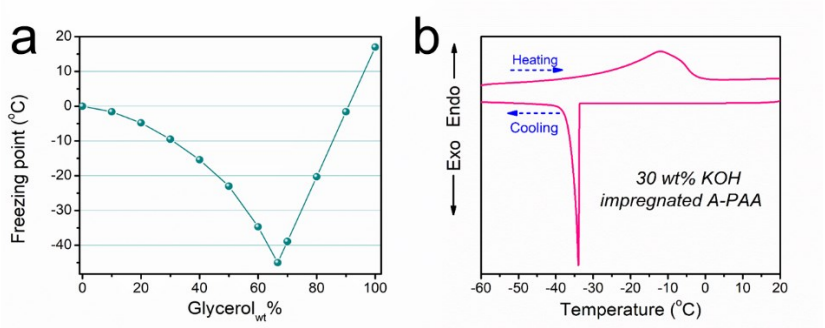

Figure S32. (a) The freezing point of the glycerol-water binary aqueous solutions with different weight percent of glycerol.[S24] (b) DSC curve of the KOH-filled A-PAA hydrogel.

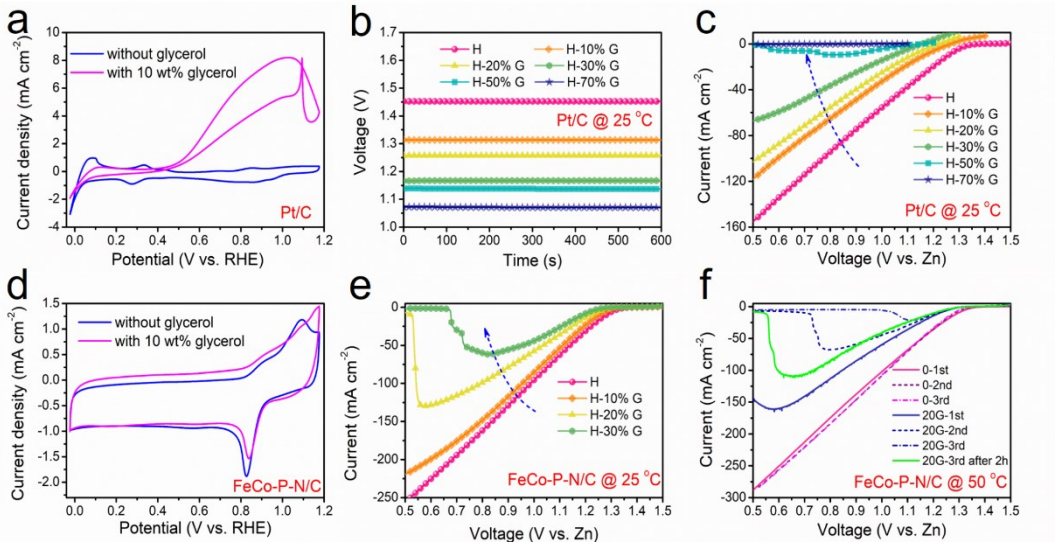

Figure S33. Influence of the glycerol content on the electrochemical performances of different catalysts and corresponding ZABs: (a) CV curves of Pt/C catalyst with or without 10 wt% glycerol in O_2 saturated 0.1 M KOH; (b) OCV of the flexible ZABs based on Pt/C catalyst; (c) discharge curves of the ZABs using different hydrogel and organohydrogel electrolytes; (d) CV curves of FeCo-P/N-F-C catalyst with or without 10 wt% glycerol in O_2 saturated 0.1 M KOH, **catalyst loading 0.3 mg cm^{-2}, scan rate 20 mV s^{-1}**; (e) discharge curves of the ZAB-Stereo using typical hydrogel and organohydrogel electrolytes under 25 °C; (f) discharging reversibility of the ZAB-Stereo using hydrogel and organohydrogel, tested under 50 °C.

Note 11: One critical limitation of the organohydrogel polyelectrolyte is that the introduced organic species will deteriorate the charge/discharge performances of the ZABs. For example, a noble metal catalyst like Pt/C is very sensitive to these small organic molecules. **Figure S33a** shows that a 10 wt% of G in KOH solution will thoroughly alter the desired ORR to parasitic glycerol oxidation reaction (GOR), as evidenced by the large oxidation current in G solution. The intermediates from GOR will substantially poison the Pt/C catalyst for ORR. As a result, the OCV of the ZABs shows a significant decline upon the deployment of organohydrogel electrolytes (**Figure S33b**). Also, the discharge curves of the battery are dramatically degenerated (even to total failure) with the presence of G (**Figure S33c**).

Though the non-noble metal-based catalyst like the FeCo-P/N-C-F used in this study can partially avoid the parasitic GOR due to its better ORR selectivity (**Figure S33d**), the electrochemical performances of the corresponding ZABs based on the organohydrogel polyelectrolytes are degraded. **Figure S33e** shows that the discharge capability of the ZABs assembled from the organohydrogel is still severely lagged behind that from the G-free polyelectrolyte. Further, the resilience of the ZAB for repeating working loadings is also seriously decayed. Even under 50 ^{o}C (where the reactants' diffusion is much faster), the 20 wt% G-based organohydrogel electrolyte can barely work twice before the sluggish recovery (**Figure S33f**). In comparison, the A-PAA-based polyelectrolyte can well retain the performance in discharging cycles. Based on these results, we can reasonably envisage that these side-effects will become more complicated during the charging (correlated to OER) of ZABs. Although a detailed analysis of the exact reaction intermediates and parasitic reactions is beyond the current study's scope, it is evident that the organohydrogels are not suitable for temperature-adaptive polyelectrolytes high-performance flexible ZABs (at least aqueous ones).

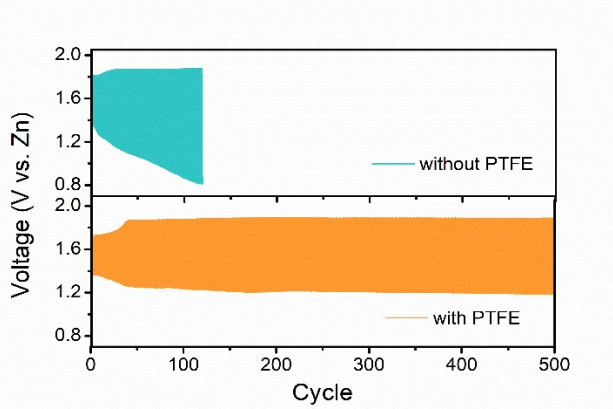

Figure S34. Cycling profiles of the ZABs assembled from the FeCo-P/N-C-F electrode with or without modification by PTFE (Teflon), tested at 2 mA cm^{-2} under 25 ^{o}C.

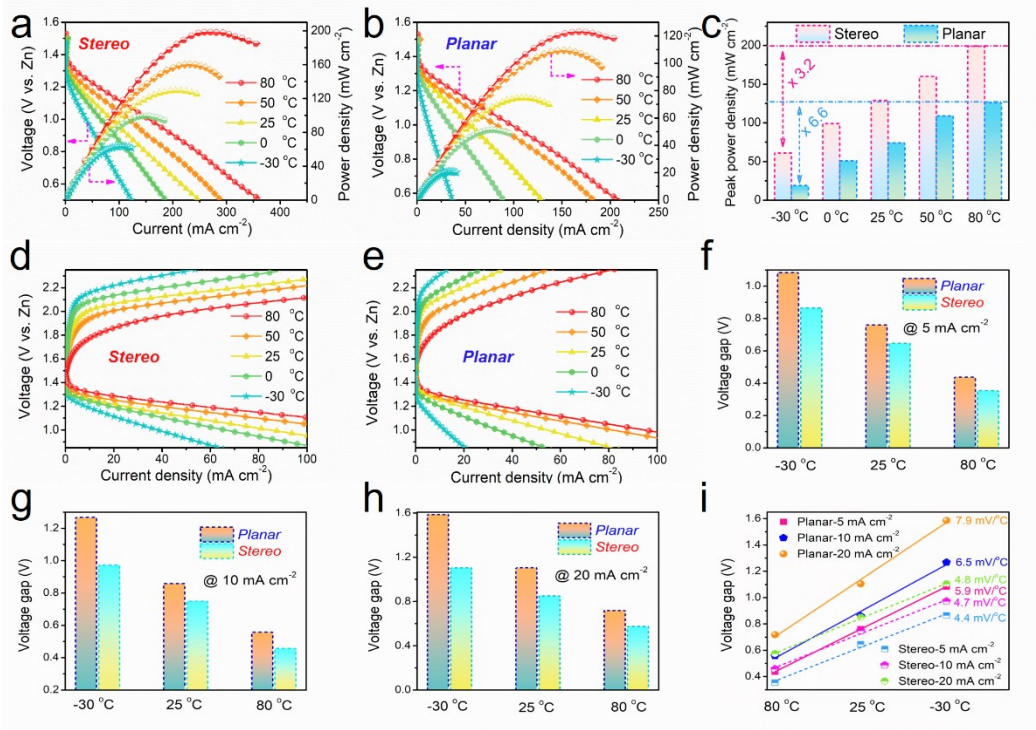

Figure S35. Electrochemical performance comparison of ZAB-Stereo and ZAB-Planar under different temperatures: discharging and power density plots from (a) ZAB-Stereo and (b) ZAB-Planar; (c) comparison of peak power density fluctuations of ZAB-Stereo and ZAB-Planar upon temperature changes; charging/discharging profiles from (d) ZAB-Stereo; (e) ZAB-Planar; voltage gaps of the two batteries at (f) 5 mA cm^{-2}; (g) 10 mA cm^{-2}; (h) 20 mA cm^{-2}; (i) voltage gap plots upon temperature decrease from 80 to -30 ^{o}C, with the voltage gap increase per unit temperature listed.

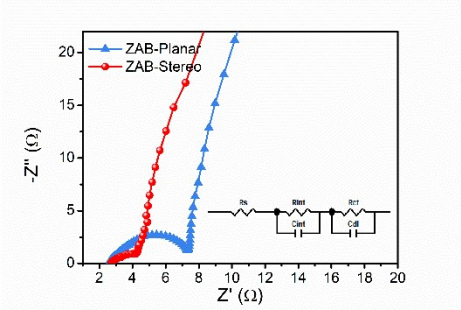

Figure S36. Nyquist plots of ZAB-Stereo and ZAB-Planar at open-circuit voltage under 25 ^{o}C, inset is the equivalent circuit.

Note 12: The Nyquist plots of flexible ZABs are typically moldeled by the equivalent circuit including five elements: bulk resitence (R_s), interfacial resistence (R_{int}), charge transfer resistence (R_{ct}), and two constant phase elements-the characteristic capacitances from the interface between the electrode and electrolyte (Q_{int} and Q_{dl}).[S25] For ZAB-Stereo and ZAB-

Planar, the R_s is 2.71 Ω and 2.58 Ω, respectively. However, the R_{int} is 1.26 Ω for ZAB-Stereo, and 3.30 Ω for ZAB-Planar, while the R_{ct} is1.68 Ω for ZAB-Stereo, 4.42 Ω for ZAB-Planar. The smaller R_{int} and R_{ct} values of the ZAB-Stereo suggest the enriched reactive TPIs from the stereoscopic electrode can indeed minimize the interfacial and charge transfer resistences.

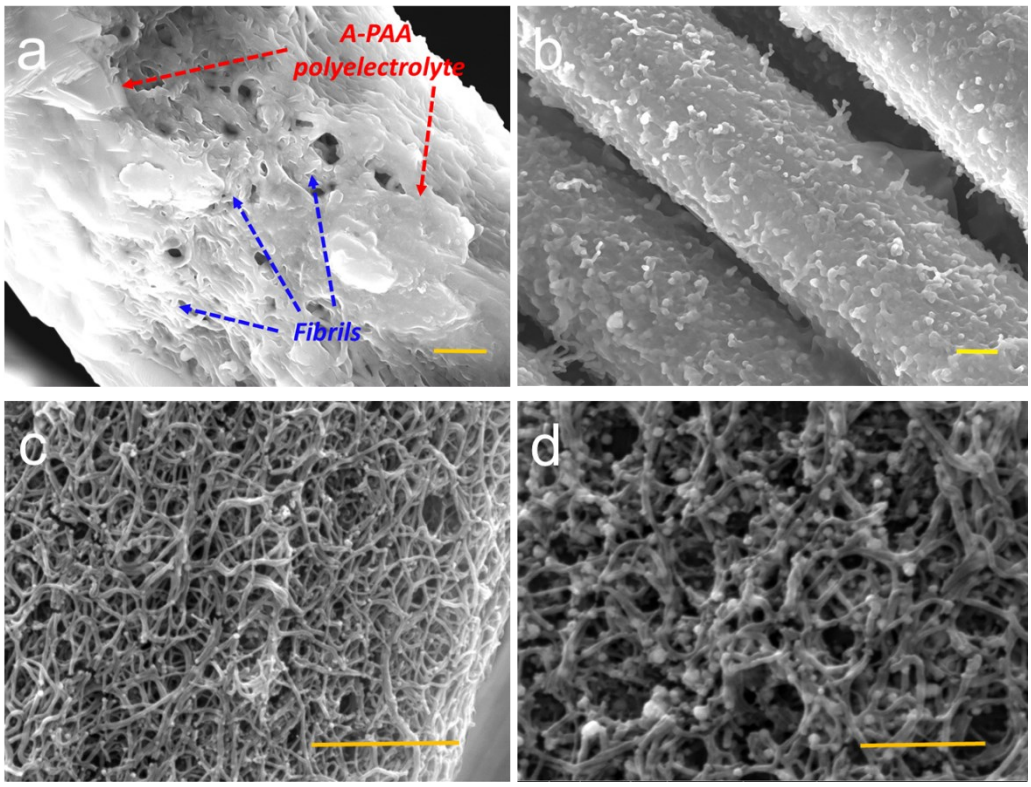

Figure S37. Morphology of different domains in FeCo-P/N-C-F electrode after 500 charge-discharge cycles in ZAB-Stereo. Scale bar: 2 μm in (a), (b) and (c), 1 μm in (d).

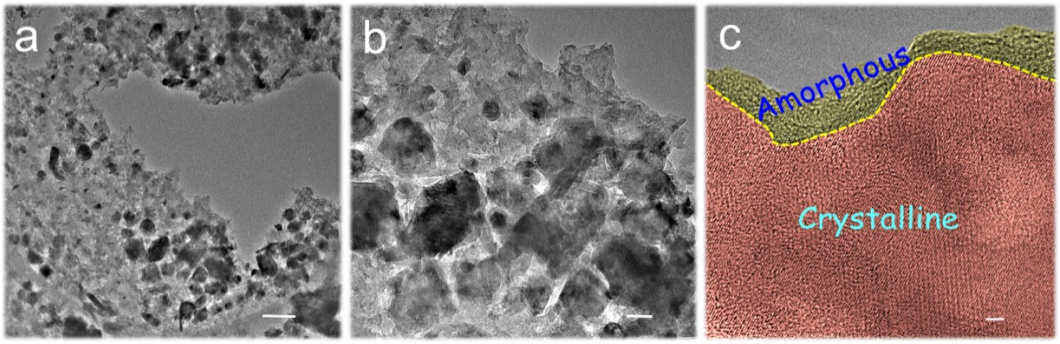

Figure S38. (a) and (b) TEM images showing the retained intimate coupling of the metal composite sites and the N-doped carbon substrate after 500 charge-discharge cycles in ZAB-Stereo. (c) An HRTEM image showing the evolved core@shell of metal sites after cycling tests in ZAB-Stereo. Scale bar: 200 nm in (a), 50 nm in (b), and 2 nm in (c).

Note 13: To review the stability of FeCo-P/N-C-F electrode after the charge-discharge cycles in ZAB, we first checked the electrode's morphology. As shown in **Figure S37**, after 500 charge-discharge cycles in ZAB-Stereo, the stereoscopic electrode well retained its morphology, satisfying for long-term use. We then further conducted TEM analyses to check metal sites. **Figure S38a** and **b** exhibit that the high contrast metal particles are still embedded in the carbon matrix, highlighting that the intimate contact between the metal sites and N-doped carbon substrate was well-preserved during the cycling. Such intimate coupling of the metal sites and the carbon substrate ensures facilitated charge transfer and avoids detachment of the active sites, which is one of the key reasons for the good stability of FeCo-P/N-C-F electrode. Moreover, the HRTEM image in **Figure S38c** reveals that the metal site shows a typical core@shell structure with a crystalline core and a thin amorphous shell. Based on the analyses in **Figure 2d-e and S20**, the metal sites also underwent a dynamic steady state of interfacial reconstruction during charge-discharge cycles in ZAB, similar to the case during OER tests (**Figure 2c**).

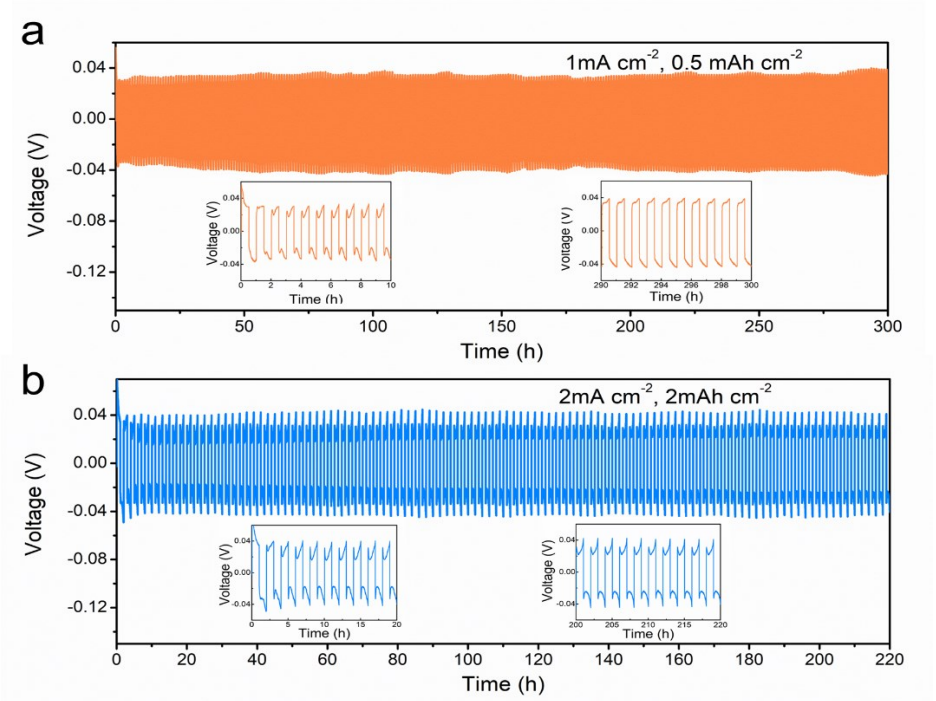

Figure S39. Galvanostatic cycling performances of Zn//Zn symmetric batteries at (a) 1 mA cm^{-2}, 0.5 mAh cm^{-2}; (b) 2 mA cm^{-2}, 2 mAh cm^{-2}.

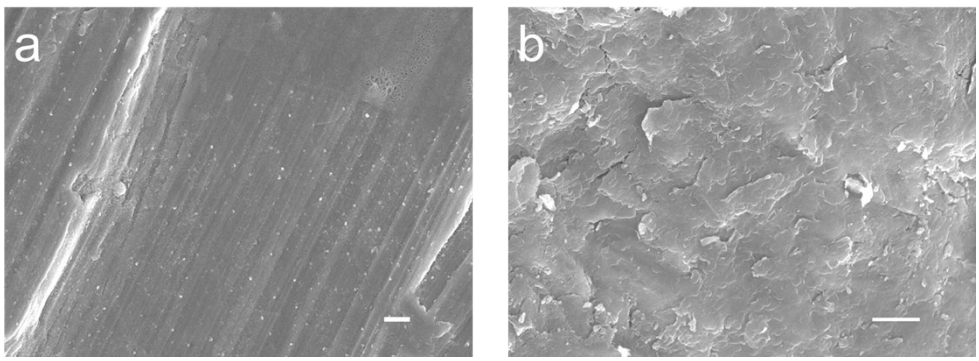

Figure S40. SEM images of (a) pristine Zn foil and (b) the Zn foil after 50 cycles at 1 mA cm^{-2}, 0.5 mAh cm^{-2}. Scale bar: 2 μm in (a) and (b).

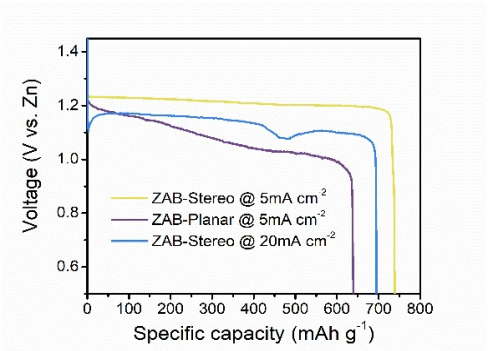

Figure S41. Specific capacity profiles of the ZAB-Stereo and ZAB-Planar at different current densities.

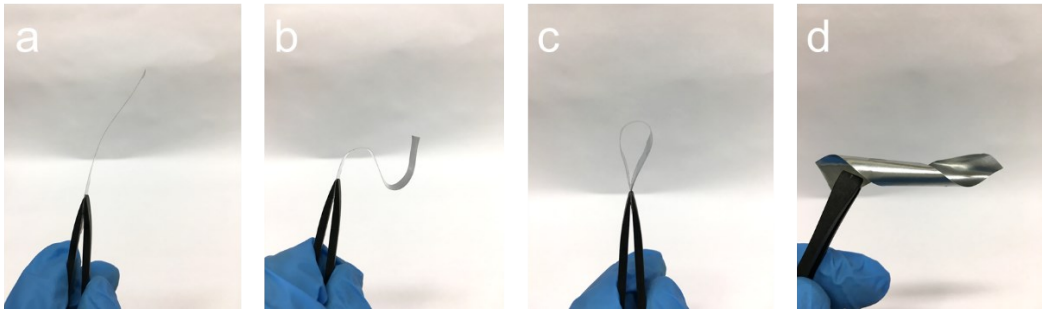

Figure S42. Photos showing the flexibility of the Zn foil (50 μm thick) used in ZABs.

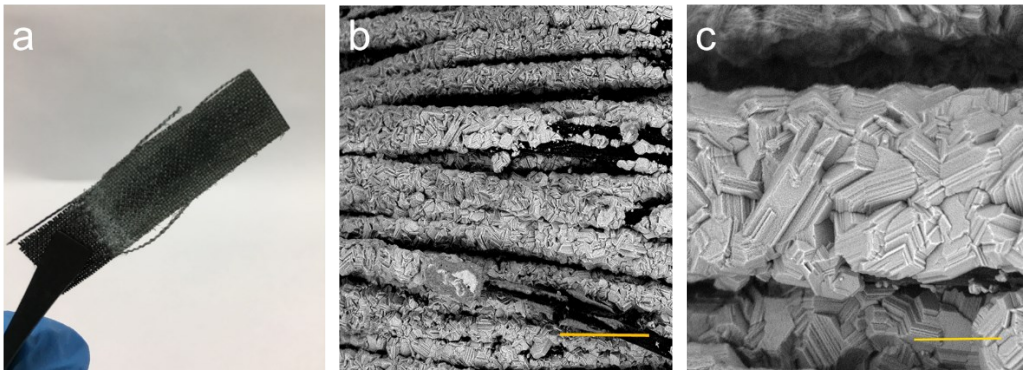

Figure S43. (a) A photo showing the Zn NS@CC electrode. (b) and (c) SEM images showing the morphology of Zn NS@CC electrode at different scales. Scale bar: 50 μm in (b) and 10 μm in (c).

Note 14: In this work, we directly used a Zn foil as the anode, which can still fulfill the basic flexible requirements (**Figure S42**) due to its small thickness of only 50 μm. We have additionally synthesized the carbon cloth-supported Zn nanosheets (by electrodeposition) electrode to fabricate flexible ZABs. As shown in **Figure S43**, the Zn nanosheets were deposited onto carbon cloth (marked as Zn NS@CC) following a reported method.[S26] The electrochemical performances of the Zn NS@CC electrode-based flexible ZAB are shown in **Figure S44**. It can be seen that due to the enlarged surface area from the nanostructured Zn, the Zn NS@CC electrode-based ZAB exhibits larger peak power density and smaller voltage gaps compared with those from the Zn foil-based counterpart.

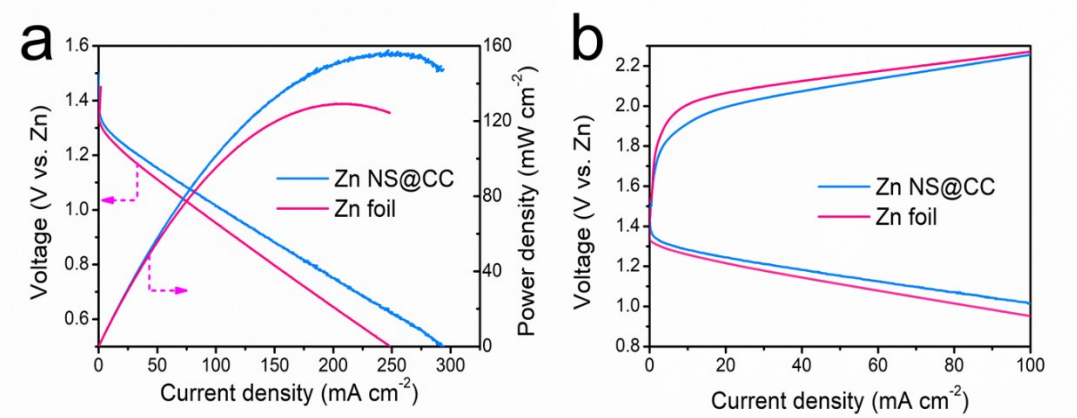

Figure S44. Comparison of electrochemical performances of flexible ZABs based on different Zn electrodes: (a) discharge and power density plots; (b) charge/discharge profiles. All tested under 25 °C.

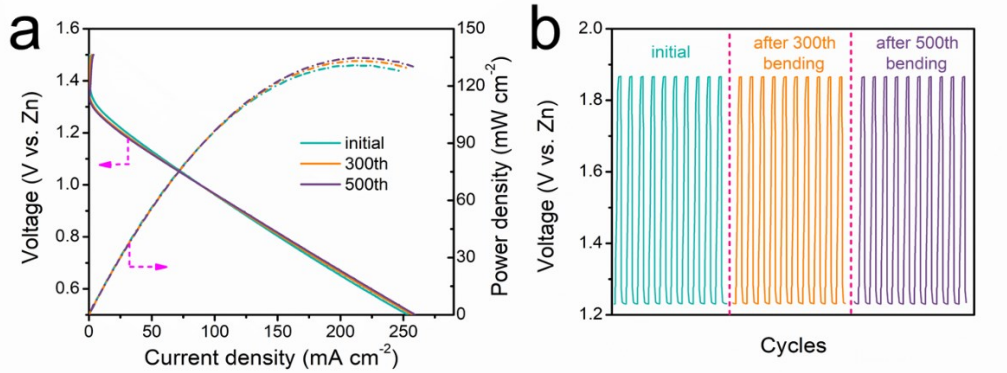

Figure S45. Flexibility tests of ZAB-Stereo: (a) polarization curves and corresponding power density plots of the battery after various times of bending (bent to 90°); (b) charge-discharge profiles of the ZAB at 2 mA cm^{-2} after different times of bending (bent to 90°).

Table S1. The correction of zero point energy and entropy of the adsorbed and gaseous species.

	ZPE(eV)	TS(eV)
*OOH	0.35	0
*O	0.05	0
*OH	0.31	0.01
*H	0.18	0.03
H_2O	0.56	0.67
H_2	0.27	0.41

Table S2. Comparison study of some recently reported self-support and powder reversible oxygen electrocatalysts in KOH electrolyte

Catalyst	Catalyst type	$E_{1/2}$ for ORR (V vs. RHE)	$E_{J=10}$ for OER (V vs. RHE)	ΔE ($E_{j=10} - E_{1/2}$) (V)	Reference
FeCo-P/N-C-F	**Self-support**	**0.85**	**1.47**	**0.62**	**This work**
Co_4N/N-C	Self-support	0.8	1.54	0.74	*J. Am. Chem. Soc.* **2016**, 138, 10226
NC-Co_3O_4/CC	Self-support	0.87	1.58	0.71	*Adv. Mater.* **2017**, 29, 1704117
NiO/CoO-NW	Self-support	0.82	1.48	0.66	*Angew. Chem. Int. Ed.* **2019**, 58, 9459
Co_3O_{4-x} HoNPs@ HPNCS	Self-support	0.83	1.57	0.74	*Angew. Chem. Int. Ed.* **2019**, 58, 13840.
Co SA/N-C	Self-support	0.88	1.63	0.75	*Adv. Mater.* **2019**, 31, 1808267
Co@NCNTA/CC	Self-support	0.86	1.51	0.65	*Small Methods,* **2020**, 4, 1900571.
$CoO_{0.87}S_{0.13}$/GN	Powder	0.83	1.59	0.76	*Adv. Mater.***2017**, 29, 1702526
Fe-N_4 SAs/NPC	Powder	0.885	1.66	0.775	*Angew. Chem., Int. Ed.* **2018**, 57, 8614
$CaMnO_3$-S	Powder	0.76	1.7	0.94	*Adv. Energy Mater.* **2018**, 1800612
Co@CoO/NCNT	Powder	0.86	1.63	0.77	*Energy Storage Mater.* **2019**, 20, 234
MnO/Co/PGC	Powder	0.78	1.60	0.82	*Adv. Mater.***2019**, 31, 1902339
Co_2FeO_4/NCNT	Powder	0.8	1.66	0.86	*Angew. Chem. Int. Ed.* **2019**, 58, 13291

CoNi-SAs/NC	Powder	0.76	1.57	0.81	*Adv. Mater.***2019**, 31, 1905622
CoO_x/N-RGO	Powder	0.896	1.60	0.704	*Adv. Mater.* **2019**, 31, 1807468
Mn/Fe-HIB-MOF	Powder	0.88	1.51	0.63	*Energy Environ. Sci.*, **2019**, 12, 727
FeCo-N-C	Powder	0.90	1.60	0.70	*Angew. Chem. Int. Ed.* **2020**, 59, 4793

Table S3. Electrochemical performance of recently reported temperature-adaptive flexible ZABs

Design strategy	Low- T limit (°C)	High-T Limit (°C)	Working – T span (°C)	Energy density retention	Peak power density (mW cm^{-2})	Cycling stability at extreme T	Ref.
Organohydrogel	-20	70	90	72.4% @ -20 °C 96.6% @ 70 °C	8.2 @ -20 °C 12.8 @ 70 °C	*100 cycles for 10 h @ -20 °C* *30 cycles for 3 h @ 70 °C*	*ACS Sustainable Chem. Eng.* 2020, 8, 11501
Hydrogel	-20	-	45	97% @ -20 °C	54.2 @ -20 °C	*72 cycles for 24 h @ -20 °C*	*ACS Appl. Mater. Inter. 2020, 12, 10, 11778*
Catalyst	-10	40	50	-	-	*≤60 cycles for 20 h @ 40 °C* *≤30 cycles for 10 h @ 40 °C*	*ChemCatChem, 2019, 11, 6002*
Catalyst	-10	80	90	36.5% @ -10 °C 34.2% @ 80 °C	-	*42 cycles for 14 h @ -10 °C* *36 cycles for 12 h @ 80 °C*	*Angew. Chem. Int. Ed.*, 2019, 58, 9459
Catalyst	-20	-	45	87.2% @ -20 °C	80.5 @ -20 °C	-	*Angew. Chem. Int. Ed.*, 2020, 59, 4793
Air-cathode structure	-30	80	110	88.6% @ -30 °C 93.2% @ 80 °C	63.6 @ -30 °C 199.1 @ 80 °C	*500 cycles for 92 h @ -30 °C* *500 cycles for 92 h @ 80 °C*	This work

References

[S1] J. Qiao, L. Xu, L. Ding, P. Shi, L. Zhang, R. Baker, J. Zhang. *Int. J. Electrochem. Sci.* 2013, **8**, 1189.

[S2] Z. Lu, W. Xu, J. Ma, Y. Li, X. Sun, L. Jiang. *Adv. Mater.* 2016, **28**, 7155-7161.

[S3] a) G. Kresse, J. Furthmüller. *Phys. Rev. B* 1996. **54**, 11169; b) G. Kresse, J. Hafner. *Phys. Rev. B* 1994. **49**, 14251.

[S4] P.E. Blöchl. *Phys. Rev. B* 1994. **50**, 17953.

[S5] a) J.P. Perdew, K. Burke, M. Ernzerhof. *Phys. Rev. Lett.* 1996, **77**, 3865; b) Y. Zhang, W. Yang. *Phys. Rev. Lett.,* 1998. **80**, 890; c) B. Hammer, L.B. Hansen, J. K. Nørskov. *Phys. Rev. B*, 1999. **59**, 7413.

[S6] S. Dudarev, et al. *Phys. Rev. B* 1998, **57**, 1505.

[S7] H. J. Monkhorst, J.D. Pack. *Phys. Rev. B* 1976, **13**, 5188.

[S8] J. K. Nørskov, et al. *J. Phys. Chem. B* 2004. **108**, 17886-17892.

[S9] J. P. Perdew, A. Ruzsinszky, G. I. Csonka, O. A. Vydrov, G. E. Scuseria, L. A. Constantin, X. Zhou, K. Burke. *Phys. Rev. Lett.* 2008, **100**, 136406.

[S10] J. C. Sancho-García, J. L. Brédas, J. Cornil. *Chem. Phys. Lett.* 2003, **377,** 63-68.

[S11] a) G. S. Chaubey, C. Barcena, N. Poudyal, C. Rong, J. Gao, S. Sun, J. P.. Liu. *J. Am. Chem. Soc*. 2007, 129, 7214; b) S. Guo, S. Zhang, L. Wu, S. Sun. *Angew. Chem*., 2012, 124, 11940; c) T. Zhou, W. Xu, et al. *Adv. Mater.* 2019, 31, 1807468.

[S12] K. Liu, C. Zhang, Y. Sun, et al. *ACS Nano* 2018, 12, 158.
[S13] a) B. Zhang, X. Zheng, et al. *Science*, 2016, **352**, 333-337; b) C. Wei, R. R. Rao, J. Peng, B. Huang, I. E. L. Stephens, M. Risch, Z. J. Xu, and Y. Shao-Horn. *Adv. Mater.* 2019, ***31***, 1806296.
[S14] W. Jiang, L. Gu, L. Li, et al. *J. Am. Chem. Soc*., 2016, 138, 3570.
[S15] S. Jin, *ACS Energy Lett.* 2017, **2**, 1937–1938.
[S16] a) H. Xu, Z. Shi, Y. Tong, G. Li. *Adv. Mater*. 2018, 30, 1705442; b) C. Liang, P. Zou, A. Nairan, et al. *Energy Environ. Sci*. 2020, 13, 86.
[S17] H. Liang, A. N. Gandi, C. Xia, et al. *ACS Energy Lett.* 2017, 2, 1035;
[S18] a) E. Fabbri, M. Nachtegaal, T. Binninger, et al. *Nat. Mater.* 2017, 16, 925; b) J. Huang, Y. Li, Y. Zhang, et al. *Angew. Chem., Int. Ed*. 2019, 58, 17458; c) Y. Duan, J. Y. Lee, S. Xi, et al. *Angew. Chem. Int. Ed*. 2021, 60, 7418; d) J. Wang, S. J. Kim, J .Liu, et al. *Nat. Catal*. 2021, 4, 212.
[S19] a) A. V. Ramosa, M. J. Guittet, J. B. Moussy. *Appl. Phys. Lett*. 2007, 91, 122107; b) N. Zhang, S. Ruan, F. Qu, et al. *Sens. Actuators B Chem.*, 2019, 298, 126887; c) Z. Shao, T. Zeng, Y. He, et al. *Chem. Eng. J.*, 2019, 359, 485.
[S20] J. Guo, C. Mao, R. Zhang, et al. *J. Mater. Chem. A*, 2017, 5, 11016.
[S21] K. He; T. T. Tsega, X. Liu, et al. *Angew. Chem. Int. Ed*. 2019, 58, 11903.
[S22] a) V. R. Stamenkovic, B. S. Mun, M. Arenz, et al. *Nat. Mater*. 2007, 6, 241; b) P. Li, M. Wang, X. Duan, et al. *Nat. Commun*. 2019, 10, 1711.
[S23] F. Meng, H. Zhong, D. Bao, J. Yan, X. Zhang, *J. Am. Chem. Soc.* 2016, **138**, 10226-10231.
[S24] a)L. B. Lane, *Ind. Eng. Chem.* 1925, **17**, 924-924; b) L. Han, K. Liu, M. Wang, K. Wang, L. Fang, H. Chen, J. Zhou, X. Lu, *Adv. Funct. Mater.* 2018, **28**, 1704195.
[S25] D. U. Lee, M. G. Park, H. W. Park, et al. *ChemSusChem* **2015,** 8, 3129.
[S26] Y. Zeng, X. Zhang, R. Qin, X. Liu, P. Fang, D. Zheng, Y. Tong, X. Lu. *Adv. Mater.* 2019, **31**, 1903675.